

A Giant Metrewave Radio Telescope search for associated H I 21 cm absorption in GHz-peaked-spectrum sources.

J. N. H. S. Aditya^{1,2*}, Nissim Kanekar^{2†}

¹*Inter-University Centre for Astronomy and Astrophysics, Pune 411007, India*

²*National Centre for Radio Astrophysics, Tata Institute of Fundamental Research, Pune 411007, India*

Accepted XXX. Received YYY; in original form ZZZ

ABSTRACT

We report the first detections of associated H I 21 cm absorption in Gigahertz-peaked-spectrum (GPS) sources at high redshifts, $z > 1$, using the Giant Metrewave Radio Telescope (GMRT). Our GMRT search for associated H I 21 cm absorption in a sample of 12 GPS sources yielded two new detections of absorption, towards TXS 1200+045 at $z = 1.226$ and TXS 1245–197 at $z = 1.275$, and five non-detections. These are only the sixth and seventh detections of associated H I 21 cm absorption in active galactic nuclei (AGNs) at $z > 1$. Both H I 21 cm absorption profiles are wide, with velocity spans between nulls of $\approx 600 \text{ km s}^{-1}$ (TXS 1200+045) and $\approx 1100 \text{ km s}^{-1}$ (TXS 1245–197). In both absorbers, the large velocity spread of the absorption and its blueshift from the AGN, suggests that it arises in outflowing neutral gas, perhaps driven by the radio jets to high velocities. We derive mass outflow rates of $\dot{M} \approx 32 M_{\odot} \text{ yr}^{-1}$ (TXS 1200+045) and $\dot{M} \approx 18 M_{\odot} \text{ yr}^{-1}$ (TXS 1245–197), comparable to the mass outflow rates seen earlier in low-redshift active galactic nuclei.

Key words: galaxies: active - quasars: absorption lines - galaxies: high redshift - radio lines: galaxies

1 INTRODUCTION

Over the last decade, it has become clear that active galactic nuclei (AGNs) play a critical role in the evolution of their host galaxies and environments (e.g. Fabian 2012). Simulations have shown that interactions between the AGN jets and the surrounding gas can regulate the growth of the host galaxy, by quenching star formation in the central regions and possibly ending the active state of the nucleus, through the effects of mechanical feedback (e.g. Hopkins et al. 2005; Springel et al. 2005; Croton et al. 2006). Recent simulations have shown that the kinetic interaction of the radio jet with interstellar gas in the AGN host galaxy provides an efficient mechanism to drive gas outflows, especially when the radio source is in its initial phase and surrounded by a porous clumpy medium (e.g. Wagner & Bicknell 2011; Wagner et al. 2012). This is because a large cocoon of disturbed and outflowing gas is created around the radio jet due to its interaction with the radio plasma, thus affecting a large region of the galaxy. AGN-driven galactic winds provide an alternate efficient mechanism of driving gas flows away from the central region and regulating star formation in the host galaxy (e.g. Veilleux et al. 2005). However, despite its ac-

knowledge importance, the ubiquity of AGN feedback, its effects on galaxy evolution, whether the feedback arises during specific phases in the AGN lifetime or is a recurrent phenomenon, and the driving mechanism of the outflows all remain open issues today (Fabian 2012).

The above feedback mechanisms involve gas flowing outwards from the AGN. Conversely, gas flows towards the central regions of the AGN host galaxy are an important source of fuel for the AGN activity; the absence of such fuel can result in the cessation of AGN activity. The kinematics of gas in AGN environments thus has important implications for galaxy evolution.

“Associated” H I 21 cm absorption studies provide an interesting probe of the presence and kinematical properties of neutral hydrogen (H I) in AGN environments (e.g. Morganti 2012). The detection rate of H I 21 cm absorption at different redshifts provides information about the availability of fuel for the AGN activity. In the case of detections of H I 21 cm absorption, the line width, the line shape, and the velocity offset relative to the AGN redshift can be used to probe conditions in the AGN environment (e.g. Geréb et al. 2015). Absorption profiles that are narrow, with widths $\lesssim 200 \text{ km s}^{-1}$, are likely to arise from clouds that are rotating in disks around the nucleus, while broader line profiles, with widths $\gtrsim 300 \text{ km s}^{-1}$, suggest the presence of highly unsettled gas, that may be interacting with the nuclear jets

* adityaj@iucaa.in

† Swarnajayanti Fellow; nkanekar@ncra.tifr.res.in

(e.g. Geréb et al. 2015). An absorption line that is redshifted from the AGN’s systemic velocity is likely to indicate neutral gas that is flowing towards the central regions, i.e. a source of fuel for the central AGN (e.g. van Gorkom et al. 1989). Conversely, absorption lines that are blueshifted from the systemic velocity are likely to indicate outflowing gas, due to either stellar outbursts or ram pressure from the AGN jets.

The detection of blueshifted and wide associated H I 21 cm absorption features can be used to probe jet-cloud interactions, and thus aid in understanding AGN-driven feedback. It is also interesting to test whether there is a preponderance of blueshifted or redshifted absorption features at a given redshift, and whether this evolves with redshift. Early studies of associated H I 21 cm absorption in the local Universe found the absorption to lie either at or redward of the AGN systemic velocity, indicating infall of neutral gas to the inner regions of the AGN host galaxy, with infall rates sufficient to fuel the nuclear activity (van Gorkom et al. 1989). More recently, a number of blueshifted associated H I 21 cm absorption lines have been detected at low and intermediate redshifts, $z < 1$, suggesting that AGN outflows play an important role in the kinematics here (e.g. Vermeulen et al. 2003; Geréb et al. 2015). Indeed, very fast H I outflows, with velocities $\gtrsim 1000 \text{ km s}^{-1}$, have been observed in a few low-redshift AGNs (IC 5063, 4C12.50, 3C293, Mrk231, etc.; e.g. Morganti et al. 1998, 2005, 2016). Very Long Baseline Interferometry (VLBI) mapping in the H I 21 cm absorption line has been used to find evidence that the radio jet is driving the H I outflow in a few cases (IC 5063, 4C12.50, 3C305, Mrk231; e.g. Oosterloo et al. 2000; Morganti et al. 2003). Equally interesting, some of these outflows (e.g. NGC 1266, Mrk231, NGC 1433, etc.; e.g. Alatalo et al. 2011; Combes et al. 2013; Dasyra et al. 2016) have been shown to have a molecular counterpart; this has important implications for their impact on both quenching of star formation in the host galaxy and the intergalactic medium, as the presence of molecular gas implies that the outflows carry even more mass than in the purely atomic case (e.g. Fiore et al. 2017).

Finally, while a number of attempts have been made to use associated H I 21 cm absorption studies to probe AGN environments at high redshifts, $z \gg 1$ (e.g. Gupta et al. 2006; Curran et al. 2013; Aditya et al. 2016), these have mostly been unsuccessful. There are at present only five known associated H I 21 cm absorbers at $z > 1$, at $z \approx 1.2$ towards 3C190 (Ishwara-Chandra et al. 2003) and TXS 1954+513 (Aditya et al. 2017), $z \approx 1.3$ towards J1545+4751 (Curran et al. 2013), $z \approx 2.6$ towards MG J0414+0534 (Moore et al. 1999), and $z \approx 3.4$ towards TXS 0902+343 (Uson et al. 1991). Indeed, the detection fraction of associated H I 21 cm absorption in compact flat-spectrum sources has been shown to have a strong dependence on both redshift and AGN ultraviolet/radio luminosity, with low detection rates at high redshifts and high luminosities (Aditya et al. 2016). It has not so far been possible to separate between redshift evolution and AGN luminosity as the primary cause of the above effect.

At low redshifts, the highest detection rate of associated H I 21 cm absorption has been found in Gigahertz Peaked Spectrum (GPS) sources (e.g. Gupta et al. 2006). GPS sources are known to be extremely compact, with

transverse sizes $\lesssim 1 \text{ kpc}$ (O’Dea 1998). It is now widely agreed that these sources correspond to the early stages of the evolution of powerful radio galaxies (e.g. Fanti et al. 1995; Readhead et al. 1996; Snellen et al. 2000). The radio-emitting region grows and expands within the interstellar medium of the host galaxy, before breaking out to become a powerful radio source. GPS sources thus appear to be good candidates to search for jet-cloud interactions, since such effects are believed to be prominent in young AGNs, where the radio emission is engulfed in the ambient gas reservoir. Further, the high detection rate of H I 21 cm absorption suggests that these may be the best targets to extend studies of associated H I 21 cm absorption to high redshifts, $z > 1$.

At present, only three of the 23 GPS sources that have been searched for associated H I 21 cm absorption lie at $z > 1$. (e.g. Vermeulen et al. 2003; Gupta et al. 2006), with no reported detections. The kinematical properties of neutral gas in the vicinity of high- z GPS sources, and the redshift evolution of their environment, thus remain open questions. We have hence put together a sample of 58 GPS sources at declinations observable with the Giant Metrewave Radio Telescope (GMRT), and whose H I 21 cm line frequencies redshift into the GMRT bands, from the GPS literature (e.g. Stanghellini et al. 1998; Labiano et al. 2007; de Vries et al. 2007a; Randall et al. 2011). The selection criteria are that the sources should have inverted spectra, with the turnover frequency lying between 300 MHz and 5 GHz (the definition of a GPS source; e.g. Labiano et al. 2007). 23 of the 58 sources have earlier searches for H I 21 cm absorption in the literature. In this paper, we report results from a GMRT search for redshifted H I 21 cm absorption in the 12 brightest GPS sources of this sample, that has yielded the first two detections of H I 21 cm absorption in GPS sources at $z > 1$.

2 OBSERVATIONS, DATA ANALYSIS AND RESULTS

2.1 The GMRT observations

Our GMRT search for associated H I 21 cm absorption from the 12 brightest GPS sources of our full sample was carried out in GMRT Cycle 29 over 2015 October – December. The GMRT L-band receivers were used for the nine targets at $z \lesssim 0.4$, and the 610 MHz receivers for the three targets at $z \approx 1.1 - 1.5$. The GMRT Software Backend (GSB) was used as the correlator for all observations, with a bandwidth of 16.7 MHz centred at the expected redshifted H I 21 cm line frequency and sub-divided into 512 channels. This yielded a velocity coverage of $\approx 3900 - 5000 \text{ km s}^{-1}$ and a velocity resolution of $\approx 7.7 - 9.8 \text{ km s}^{-1}$, for the sources at $z < 0.4$, and a velocity coverage of $\approx 7600 - 8000 \text{ km s}^{-1}$ and a velocity resolution of $\approx 14.8 - 15.6 \text{ km s}^{-1}$ for the sources at $z \approx 1.1 - 1.5$. Observations of the standard primary calibrators 3C48, 3C147 and/or 3C286 were used to calibrate the flux density scale and the system passband, while observations of nearby compact sources were used for phase (and, in some cases, passband) calibration. The on-source times were $\approx 1 \text{ hour}$ apiece.

The initial spectra of two sources, TXS 1200+045 and TXS 1245–197, showed tentative detections of H I 21 cm absorption. These sources were hence re-observed in 2016 August, with a similar observing setup (i.e. the GSB as the

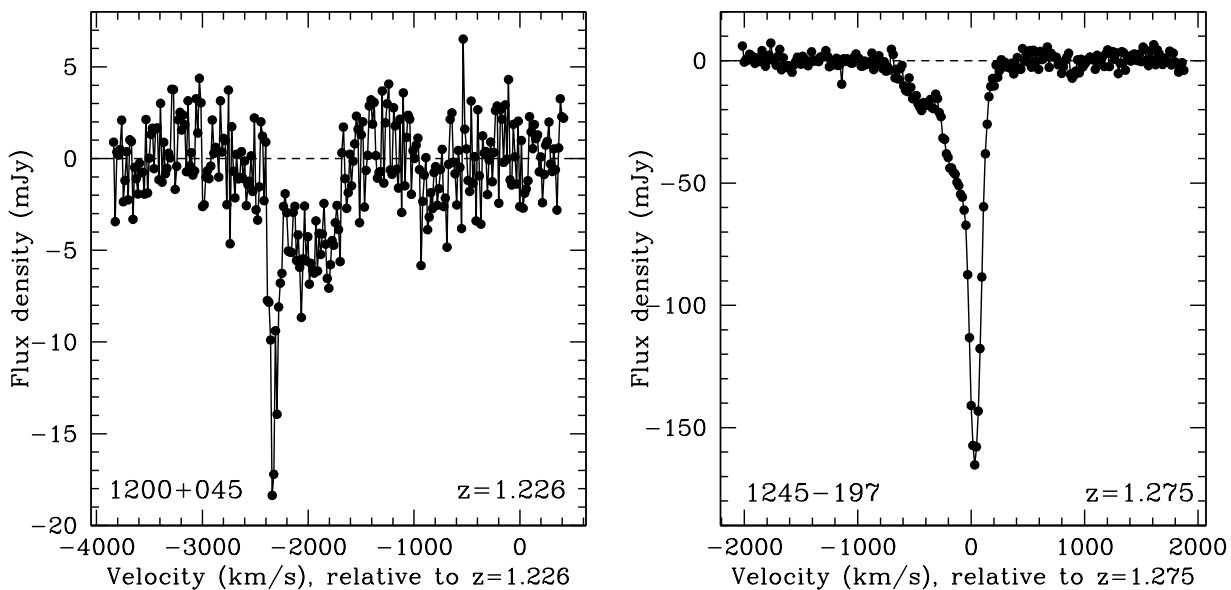


Figure 1. [A] (left panel): The GMRT HI 21 cm absorption spectrum towards TXS 1200+045, at $z = 1.226$, from August 2016. [B] (right panel): The GMRT HI 21 cm absorption spectrum towards TXS 1245-197, at $z = 1.275$, from August 2016 and June 2017.

correlator, a bandwidth of 16.7 MHz and 512 channels, and standard flux density, passband and phase calibration), but with on-source times of ≈ 2 hours apiece. In both cases, however, the observing band was centred at the line frequency of the putative absorption feature, i.e. ≈ 644.33 MHz for TXS 1200+045 and ≈ 624.35 MHz for TXS 1245-197.

Finally, the new GMRT spectrum of TXS 1245-197 showed evidence of wide HI 21 cm absorption, in addition to the strong narrow component seen in the original spectrum. We hence re-observed this source in 2017 June, to confirm the wide feature, with the same observing setup and procedure as that in 2016 August, but with a total on-source time of 4 hours.

2.2 Data analysis

The GMRT data were analysed in “classic” AIPS, using standard procedures. The data were first inspected and edited, to remove non-working antennas and time-specific bad data, usually arising due to intermittent radio frequency interference (RFI). The antenna bandpasses were determined using the data on the flux calibrators. After calibration of antenna-dependent gains and bandpass shapes, an iterative self-calibration procedure was followed for each target source. Typically, this consisted of 3–4 rounds of phase-only self-calibration and imaging, followed by 1–2 rounds of amplitude-and-phase self-calibration and imaging. At the end of the above procedure, the visibility data were again inspected, and further edited to remove any corrupted data, after which the self-calibration was repeated. This iterative procedure was carried out until it yielded an image that did not improve upon further self-calibration and data editing. The final continuum image was then subtracted out from the calibrated spectral-line visibilities. Any remaining continuum emission was removed by fitting a first-order polynomial to line-free channels in each visibility spectrum,

and subtracting this out. The residual visibilities were then shifted to the heliocentric reference frame, using the AIPS task CVEL, and then imaged to obtain the final spectral cube. The spectra were obtained via a cut through the “dirty” cube at the location of the target source.

The spectra of 5 sources from our GPS sample, TXS 1540-077 at $z = 0.172$, TXS 0320+053 at $z = 0.179$, TXS 1151-348 at $z = 0.258$, TXS 0019-000 at $z = 0.305$, and TXS 0240-217 at $z = 0.314$, show a clear ripple across the observing band. Attempts to excise these ripples by careful data editing were unsuccessful. Wide-band RFI features, spanning $\approx 50 - 80$ channels, were also visible in $\approx 70\%$ of the data in these sources, making it impossible to obtain clean spectra. We will hence exclude these 5 GPS sources from our sample, and from the later discussion.

2.3 Results

The seven GPS sources with RFI-free spectra were found to be compact in the GMRT continuum images (angular resolution $\approx 7 - 10''$) at the respective redshifted HI 21 cm line frequencies. The task JMFIT was hence used to fit a single-Gaussian model to a small region around each source, to estimate its flux density. Table 1 lists the measured flux densities of the seven sources. The listed flux densities at the redshifted HI 21 cm line frequencies of the remaining 5 sources, whose data were corrupted by RFI, were obtained by interpolating between the 1.4 GHz (from the FIRST or NVSS surveys; Becker et al. 1995; Condon et al. 1998) and 325/365 MHz (from the WENSS or Texas surveys; Douglas et al. 1996; Rengelink et al. 1997) flux densities from the literature.

We obtained two new detections and 5 non-detections of associated HI 21 cm absorption from our 7 GPS targets. The HI 21 cm absorption spectra of the detections and non-detections are shown in Figures 1 and 2, respectively, in

Table 1. The 12 GPS sources of this paper, in order of increasing redshift.

Name	z	$\nu_{21\text{ cm}}^a$	Vel. cov.	Res.	S_ν	ΔS	$\int \tau dV^b$	N_{HI}^b
		MHz	km/s	km/s	mJy	mJy	km s $^{-1}$	$\times 10^{21}$ cm $^{-2}$
B3 0801+437	0.123	1264.8	3942.4	15.4	407.7 ± 0.1	1.42	< 0.58	< 1.1
TXS 1540-077	0.172	1211.9	4147.2	16.2	1525.9^d	—	—	—
TXS 0320+053	0.179	1204.7	4147.2	16.2	3159.9^d	—	—	—
TXS 1819+671	0.221	1163.3	4300.8	16.8	434.1 ± 0.2	1.74	< 0.85	< 1.5
TXS 1151-348	0.258	1129.0	4454.4	17.4	4650.6^d	—	—	—
TXS 1108+201	0.299	1093.4	4556.8	17.8	1448.7 ± 0.2	3.93	< 0.44	< 0.81
TXS 0019-000	0.305	1088.4	4608.0	18.0	2985.7^d	—	—	—
TXS 0240-217	0.314	1080.9	4659.2	18.2	1229.9^d	—	—	—
TXS 0507+179	0.416	1003.1	5017.6	19.6	504.2 ± 0.3	1.11	< 0.41	< 0.75
TXS 2121-014	1.158	658.2	7628.8	29.8	2095.2 ± 0.4	3.56	< 0.38	< 0.69
TXS 1200+045	1.226	638.1	7833.6	15.3 ^c	1675.2 ± 0.4	1.98	2.52 ± 0.12	4.59 ± 0.22
TXS 1245-197	1.275	624.3	7987.2	15.6 ^c	8302.2 ± 0.6	3.62	4.542 ± 0.043	8.280 ± 0.078

Notes to the table:

^a $\nu_{21\text{ cm}}$ is the redshifted H I 21 cm line frequency.^b For H I 21 cm non-detections, the 3σ upper limits on the velocity-integrated H I 21 cm optical depth and the H I column density assume a line FWHM of 100 km s $^{-1}$ and a spin temperature of 1000 K. The 3σ optical depth limits have been computed after smoothing each spectrum to a resolution of 100 km s $^{-1}$.^c The quoted velocity resolution is without Hanning-smoothing and re-sampling.^d The flux density of the source at the redshifted H I 21 cm line frequency was estimated by interpolating between the 1.4 GHz (from the FIRST or NVSS surveys; [Becker et al. 1995](#); [Condon et al. 1998](#)) and the 325/365 MHz (from the WENSS or Texas surveys; [Douglas et al. 1996](#); [Rengelink et al. 1997](#)) flux densities from the literature.

order of increasing redshift. All spectra show flux density (in mJy, after subtracting out the source flux density) plotted against velocity (in km s $^{-1}$), relative to the source redshift. The spectra of the non-detections in Figure 2 have been Hanning-smoothed and re-sampled to the velocity resolutions listed in Table 1. For the H I 21 cm detection towards TXS 1200+045, the spectrum shown in Figure 1 is from the second observing run in August 2016, which has a higher sensitivity. For the second H I 21 cm detection, towards TXS 1245-197, the spectrum shown in the figure was obtained by combining the spectra from August 2016 and June 2017, with appropriate weights.

Table 1 summarizes the results from our GMRT observations. The columns of this table are (1) the AGN name, (2) the AGN redshift, z , (3) the redshifted H I 21 cm line frequency, $\nu_{21\text{ cm}}$, in MHz, (4) the velocity coverage around the redshifted H I 21 cm line frequency, in km s $^{-1}$, (5) the velocity resolution, in km s $^{-1}$, after Hanning-smoothing and re-sampling, (6) the AGN flux density, S_ν , in mJy, measured at the observing frequency listed in column (3), (7) the root-mean-square (RMS) noise ΔS on the final H I 21 cm spectrum at the velocity resolution of column (5), (8) the integrated H I 21 cm optical depth $\int \tau dV$ in km s $^{-1}$, or, for non-detections, the 3σ upper limit on $\int \tau dV$, (9) the H I column density N_{HI} in cm $^{-2}$, or, for non-detections, the 3σ upper limit on N_{HI} , assuming a gas spin temperature of 1000 K. We emphasize that, for non-detections, the upper limits on the integrated H I 21 cm optical depth and the H I column density assume that the line profile has a Gaussian shape with a full-width-at-half-maximum of 100 km s $^{-1}$, with the 3σ optical depth limit computed at the same velocity resolution. For detections, the RMS noise values on the final spectra were obtained over line-free channels. The assumed spin temperature of 1000 K was used for consistency with the

literature (e.g. [Morganti et al. 2005](#)); however, we note, in passing, that high spin temperatures are expected for neutral gas located close to a bright radio source (e.g. [Maloney et al. 1996](#)).

The two new detections of associated H I 21 cm absorption are towards TXS 1200+045, at $z = 1.226$, and TXS 1245-197 at $z = 1.275$. TXS 1200+045 is compact in the GMRT 638 MHz image, with a peak flux density of 1675.2 ± 0.4 mJy (from JMFIT). The GMRT H I 21 cm absorption spectrum towards the source from 2016 August is displayed in the left panel of Figure 1. The spectrum has two distinct features, narrow deep absorption at ≈ -2300 km s $^{-1}$ relative to the AGN redshift, and wide, weak absorption extending over ≈ 500 km s $^{-1}$ over ≈ -2200 km s $^{-1}$ to ≈ -1700 km s $^{-1}$. Both features were clearly detected in the spectra taken at both observing epochs, and in both polarizations. Both the narrow and the wide features seen in the spectrum are hence likely to be real. The integrated H I 21 cm optical depth of the absorption profile is 2.52 ± 0.12 km s $^{-1}$, which implies a high H I column density of $N_{\text{HI}} = (4.59 \pm 0.22) \times (T_s/1000\text{ K}) \times 10^{21}\text{ cm}^{-2}$, for an assumed spin temperature of 1000 K and a covering factor of unity.

TXS 1245-197 is also compact in the GMRT 624 MHz image, with a peak flux density of 8302.2 ± 0.6 mJy, (from JMFIT). The GMRT H I 21 cm absorption spectrum is displayed in the right panel of Figure 1; this was obtained by averaging the spectra from August 2016 and June 2017. We note that the wide absorption feature was detected in both observing runs, with the same depth, and conclude that it is very likely to be real. The integrated H I 21 cm optical depth is 4.542 ± 0.043 km s $^{-1}$; this implies a high H I column density, $N_{\text{HI}} = (8.280 \pm 0.078) \times (T_s/1000\text{ K}) \times 10^{21}\text{ cm}^{-2}$, for an

assumed spin temperature of 1000 K and a covering factor of unity.

3 DISCUSSION

3.1 TXS 1200+045, $z = 1.226$

While TXS 1200+045 is unresolved in our GMRT 638 MHz continuum image, the 1.6 GHz VLBI image of this source shows a clear three-component structure (Liu et al. 2007). The three VLBI components have very different flux densities at 1.6 GHz (850 mJy, 81 mJy and 35 mJy in components A, B and C, respectively; Liu et al. 2007), with component A containing $\approx 90\%$ of the total VLBI flux density. It is not clear whether the three VLBI emission components arise from a core and two lobes or from a one-sided core-jet structure. We note that component-A, the brightest of the three VLBI components, lies at one end of the structure; this may suggest that the source has a core-jet structure.

The GMRT H I 21 cm absorption profile towards TXS 1200+045 in the left panel of Figure 1 has a peak line depth of ≈ 20 mJy. The absorption appears likely to arise against component-A, the strongest of the three VLBI components, as the low flux density of the other two components (< 100 mJy at 1.6 GHz; Liu et al. 2007) would imply a high H I 21 cm opacity to produce the observed H I 21 cm absorption.

The deepest H I 21 cm absorption feature in the GMRT spectrum is significantly blueshifted from the AGN redshift of $z = 1.22597 \pm 0.00084$ (e.g. Hewett & Wild 2010), by ≈ 2300 km s $^{-1}$. We note that the new Data Release-13 of the Sloan Digital Sky Survey (SDSS-DR13) lists the AGN redshift as $z = 1.22429 \pm 0.00043$, slightly lower than that of Hewett & Wild (2010), although consistent within 2σ errors. Using the SDSS-DR13 redshift would yield a difference of ≈ 2100 km s $^{-1}$ between the peak of the H I 21 cm absorption and the AGN systemic velocity, and would thus not significantly alter our results. This suggests that the absorption arises in outflowing gas, either driven by a galactic wind or mechanically pushed by the radio jet to very high velocities. The secondary feature in the spectrum, the wide, weak absorption spanning ≈ 500 km s $^{-1}$, suggests the presence of disturbed gas, possibly due to a jet-cloud interaction.

In passing, we note that the large velocity offset between the H I 21 cm absorption and the AGN redshift raises the possibility that the absorption might arise in an intervening galaxy, rather than in gas associated with the AGN. We consider this unlikely because the velocity spread between nulls of the H I 21 cm absorption is ≈ 600 km s $^{-1}$, far larger than has ever been seen in an intervening galaxy (the H I 21 cm velocity spreads in intervening high- z absorbers are typically $\approx 30 - 150$ km s $^{-1}$; e.g. Wolfe et al. 1982, 1985; Kanekar et al. 2006, 2007, 2009; Gupta et al. 2012; Kanekar 2014). The observed velocity spread in TXS 1200+045 is much more typical of velocity spreads seen in associated H I 21 cm absorbers (e.g. Morganti et al. 2005).

3.2 TXS 1245–197, $z = 1.275$

Our sample of GPS sources was selected based on the criterion that the sources have inverted spectra, with the

turnover frequency lying between 300 MHz and 5 GHz (e.g. Labiano et al. 2007). The inverted spectrum in a GPS source is believed to arise due to synchrotron self-absorption in a compact radio emission region, probably in the early stages of AGN evolution. TXS 1245–197 has an observed turnover frequency of ≈ 400 MHz, while the turnover frequency in the rest frame of the source is ≈ 900 MHz; its spectral characteristics are those of a normal GPS source.

Curiously, the VLBI 2.3 GHz and 8.6 GHz images of TXS 1245–197 (Sokolovsky et al. 2011) show two prominent parsec-scale radio lobes, along with a faint extended structure. Sokolovsky et al. (2011) found the two lobes to have comparable flux densities at both 2.3 and 8.6 GHz, and to have steep spectra between the two frequencies, with spectral indices of -0.72 and -0.59 . The authors hence classified the source as a Compact Symmetric Object (CSO), as the steep spectra make it unlikely that either source component arises from a compact core. CSOs are powerful extragalactic radio sources that show emission on both sides of an AGN, and have sizes < 1 kpc (e.g. Wilkinson et al. 1994). Relativistic beaming is believed to be small or non-existent in these objects owing to their orientation close to the plane of the sky. Hence, the two brightest VLBI source components in TXS 1245–197 are likely to correspond to parsec-scale lobes at the ends of VLBI-scale jets, with the core remaining undetected at radio frequencies.

If the steep spectra of the two compact components of the 2.3 GHz and 8.6 GHz VLBI images (Sokolovsky et al. 2011) extend to low frequencies, these components would dominate the 624 MHz flux density of TXS 1245–197. The radio core is faint at 2.3 GHz and is likely to have an inverted or flat spectrum; it is hence unlikely to contribute significantly to the 624 MHz emission detected with the GMRT. As such, the detected H I 21 cm absorption is likely to arise against one or both of the radio lobes detected in the VLBI image. The H I 21 cm absorption profile has a width of ≈ 325 km s $^{-1}$ between 20% points, but has a wide, weak wing extending ≈ 800 km s $^{-1}$ blueward of the AGN redshift. A wide wing also extends ≈ 300 km s $^{-1}$ redward of the AGN redshift, suggesting that the neutral gas may be interacting with the AGN jets. The large velocity spread of the blueshifted absorption suggests that the bulk of the absorption may arise in outflowing neutral gas from the AGN, possibly detected against both radio lobes, as has been observed at lower redshifts (e.g. Morganti et al. 2005).

3.3 Mass outflow rates

Both our H I 21 cm absorbers show clear evidence for wide, blueshifted absorption, suggestive of outflowing neutral gas. Assuming that the outflow is driven by a mass-conserving free wind, the mass outflow rate \dot{M} for neutral gas is given by (Heckman 2002; Morganti et al. 2005)

$$\dot{M} = 30 \cdot \left[\frac{\Omega}{4\pi} \right] \cdot \left[\frac{r_{\star}}{1 \text{ kpc}} \right] \cdot \left[\frac{N_{\text{HI}}}{10^{21} \text{ cm}^{-2}} \right] \cdot \left[\frac{V}{300 \text{ km/s}} \right] M_{\odot} \text{ yr}^{-1}, \quad (1)$$

where V is the outflow velocity with which the gas flows into a solid angle Ω from a minimum radius r_{\star} . Following Morganti et al. (2005), the solid angle Ω has been assumed to be π radians, while the outflow velocity has

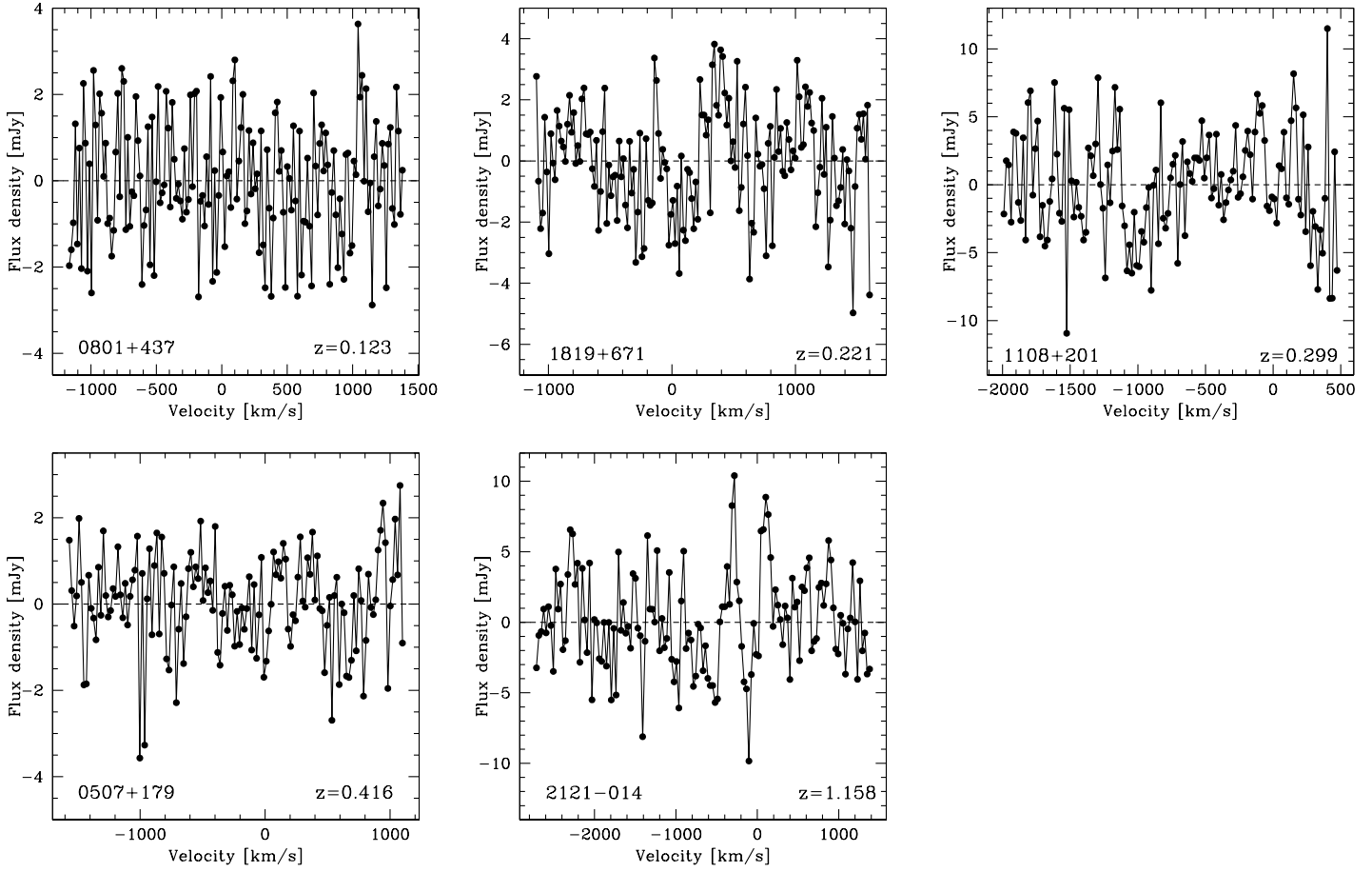


Figure 2. The GMRT H I 21 cm absorption spectra of the 5 GPS sources with non-detections of H I 21 cm absorption.

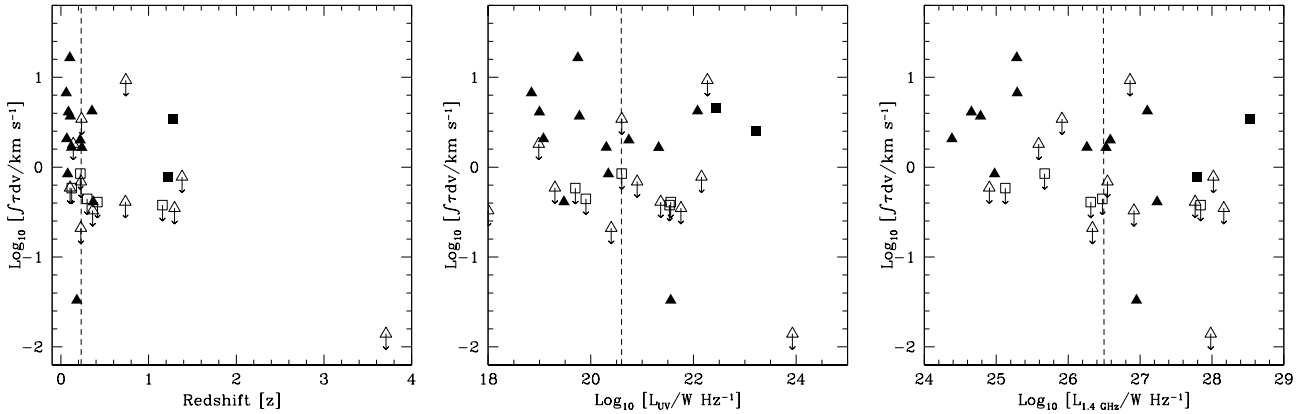


Figure 3. The integrated H I 21 cm optical depths of the sample of 30 GPS sources, plotted as a function of [A] redshift, [B] rest-frame 1216 UV luminosity, and [C] rest-frame 1.4 GHz radio luminosity. The 7 sources observed by us using the GMRT are shown as squares, while the 23 literature sources are shown by triangles. Filled symbols indicate detections of H I 21 cm absorption, while open symbols indicate upper limits on the H I 21 cm optical depth. The dashed vertical line in each panel indicates the median value of the abscissa, $z_{med} = 0.23$, $L_{UV,med} = 10^{20.6} W Hz^{-1}$, and $L_{1.4 GHz,med} = 10^{26.5} W Hz^{-1}$.

Table 2. The 30 GPS sources with H I 21 cm absorption searches, including 7 from this study and 23 from the literature, listed in order of increasing redshift. The columns of the table are (1) the AGN name, (2) the AGN redshift, (3) the integrated H I optical depth, or, for non-detections, the 3σ upper limit to this quantity, assuming a Gaussian profile with a line FWHM of 100 km s^{-1} , (4) the logarithm of the AGN luminosity L_{UV} (in $W \text{ Hz}^{-1}$) at a rest-frame wavelength of 1216 \AA , i.e. $L'_{\text{UV}} = \log[L_{\text{UV}}/(W \text{ Hz}^{-1})]$, (5) the logarithm of the AGN luminosity $L_{1.4 \text{ GHz}}$ (in $W \text{ Hz}^{-1}$) at a rest-frame frequency of 1.4 GHz , i.e. $L'_{1.4 \text{ GHz}} = \log[L_{1.4 \text{ GHz}}/(W \text{ Hz}^{-1})]$, (6, 7) the two UV or optical wavebands and the measured magnitudes therein, that were used to infer the AGN rest-frame 1216 \AA UV luminosity, (8) Ref. H I, the references for searches for associated H I absorption in the literature, and (9) Ref. UV, the references for the optical/UV fluxes that were used to infer the rest-frame 1216 \AA luminosity. See the main text for details on the computation of the AGN UV luminosity.

Source	z	$\int \tau dV^a$ km s^{-1}	L'_{UV}^b	$L'_{1.4 \text{ GHz}}^c$	Band 1 ^d mag	Band 2 ^d mag	Ref. ^e H I	Ref. ^f UV
TXS 0116+319	0.060	5.92 ± 0.13	18.85	25.29	NUV=20.5	B=16.7	5	1,2
B3 1315+415	0.066	2.10 ± 0.33	19.08	24.38	NUV=21.7	u=20.1	4	1,3
TXS 1404+286	0.077	0.84 ± 0.16	20.34	24.98	FUV=20.2	NUV=18.4	7	1,1
TXS 0902+468	0.085	4.10 ± 0.51	19.00	24.65	u=18.5	g=16.6	4	4,4
TXS 1946+708	0.101	15.8 ± 4.6	19.75	25.29	B=18.3	R=16.4	10	2,2
TXS 0729+562	0.104	< 0.59	19.30	24.90	B=16.3	R=13.4	4	2,2
GB6 J1247+6723	0.107	3.70 ± 0.27	19.78	24.78	FUV=22.9	NUV=22.6	2	1,1
TXS 1345+125	0.122	1.66 ± 0.09	20.30	26.26	NUV=19.7	B=17.0	7	1,5
B3 0801+437	0.123	< 0.58	19.70	25.13	NUV=22.7	B=17.8	11	1,2
TXS 1601-222	0.141	< 1.8	18.99	25.59	B=20.8	R=18.8	7	2,2
PKS 1934-63	0.181	0.03 ± 0.01	21.56	26.95	NUV=21.8	B=17.2	6	1,2
PKS 0428+20	0.219	2.0	20.74	26.59	B=20.4	R=18.6	1	2,2
TXS 1819+671	0.221	< 0.85	20.60	25.67	NUV=22.1	B=18.9	11	1,2
TXS 0941-080	0.228	< 0.69	20.90	26.55	FUV=21.8	NUV=21.6	1	1,1
TXS 2021+614	0.230	< 0.21	20.40	26.34	B=19.3	R=17.5	1	2,2
TXS 0554-026	0.235	< 3.4	20.60	25.92	B=18.3	R=16.5	1	2,2
TXS 2352+495	0.240	1.7	21.32	26.53	B=18.3	V=17.7	1	8,8
TXS 1108+201	0.299	< 0.44	19.90	26.48	u=21.8	g=20.9	11	4,4
TXS 2050+364	0.354	4.2	22.08	27.10	B=18.0	R=17.2	1	2,2
TXS 1117+146	0.362	< 0.33	18.01	26.92	u=23.9	g=21.8	1	3,3
TXS 1323+321	0.368	0.41	18.50	27.24	u=22.9	g=20.5	1	3,3
TXS 0507+179	0.416	< 0.41	21.56	26.31	B=20.2	R=19.0	11	2,2
8C 2342+821	0.735	< 0.41	21.36	27.77	B=21.4	R=20.0	1	2,2
TXS 2149+056	0.740	< 9.3	22.27	26.86	NUV=22.4	R=20.2	9	1,7
TXS 2121-014	1.158	< 0.38	21.53	27.84	NUV=23.9	R=23.3	11	1,5
TXS 1200+045	1.226	2.52 ± 0.12	23.21	27.80	NUV=20.4	u=18.9	11	1,3
TXS 1245-197	1.275	4.542 ± 0.043	22.44	28.52	NUV=22.1	B=21.8	11	1,6
TXS 1518+046	1.296	< 0.35	21.76	28.17	u=23.2	g=23.1	7	6,6
TXS 2055+055	1.381	< 0.78	22.16	28.02	NUV=23.2	R=23.4	7	1,7
TXS 1351-018	3.707	< 0.014	23.93	27.98	g=20.2	r=19.3	8	3,3

Notes to the table:

^a The integrated H I 21 cm optical depth or, for H I 21 cm non-detections, the 3σ limit to the H I 21 cm optical depth, in km s^{-1} , assuming a line FWHM of 100 km s^{-1} .

^b The inferred 1216 \AA UV luminosity, obtained by extrapolating from measurements in two nearby optical or UV bands (following the procedure of Curran et al. (2008)).

^c The rest-frame 1.4 GHz radio luminosities.

^d The measurements at the two UV/optical wavebands that were used to infer the 1216 \AA UV luminosities.

^e References for the associated H I 21 cm absorption searches: (1) Vermeulen et al. 2003; (2) Saikia et al. 2007; (3) Pihlström et al. 2003; (4) Chandola et al. 2011; (5) van Gorkom et al. 1989; (6) Véron-Cetty et al. 2000; (7) Gupta et al. 2006; (8) Curran et al. 2008; (9) Carilli et al. 1998; (10) Peck et al. 1999. (11) This work.

^f References for the ultraviolet, optical and infrared band measurements, that were used to obtain the inferred 1216 \AA luminosities (following the procedure of Curran & Whiting (2010)): (1) Bianchi et al. 2014, (2) Monet et al. 2003, (3) Abazajian et al. 2009, (4) Abazajian et al. 2005, (5) Surace & Sanders 2000, (6) Adelman-McCarthy et al. 2008, (7) de Vries et al. 2007b, (8) Zacharias et al. 2004.

^g The first and second entries correspond to the 1st and 2nd UV/optical bands, respectively.

Note: The typical uncertainties on measurements in the different UV, optical and near-IR wavebands are (1) 0.1 mag (NUV), (2) 0.2 mag (FUV), (3) 0.05 mag (u), (4) 0.3 mag (B), (5) 0.2 mag (V), (6) 0.01 (r), (7) 0.3 mag (R).

been assumed equal to half the Full-Width-at-Zero-Intensity (FWZI), relative to the AGN systemic velocity (i.e. half the velocity width from the outer edge of the blueshifted H I 21 cm absorption to the AGN systemic velocity); this corresponds to $\approx 1200 \text{ km s}^{-1}$ for TXS 1200+045 and $\approx 500 \text{ km s}^{-1}$ for TXS 1245–197. The radius is assumed to be equal to half the linear size of the detected low-frequency VLBI emission; this has angular extents of $\approx 75 \text{ mas}$ (TXS 1200+045; Liu et al. 2007) and $\approx 40 \text{ mas}$ (TXS 1245–197; Sokolovsky et al. 2011), corresponding to linear extents of $\approx 458 \text{ pc}$ (TXS 1200+045) and $\approx 340 \text{ pc}$ for TXS 1245–197. We hence use $r_* \approx 230 \text{ pc}$ (TXS 1200+045) and $r_* \approx 170 \text{ pc}$ (TXS 1245–197). Note that the derived mass outflow rate also depends critically on the assumed spin temperature; our assumed spin temperature of 1000 K allows a direct comparison with the low- z results of Morganti et al. (2005). This yields mass outflow rates of $\dot{M} \approx 32 \text{ M}_\odot \text{ yr}^{-1}$ (TXS 1200+045) and $\dot{M} \approx 18 \text{ M}_\odot \text{ yr}^{-1}$ (TXS 1245–197). These lie in the middle of the range of mass outflow rate estimates from similar studies at low redshifts, $\dot{M} \approx 1 - 50 \text{ M}_\odot \text{ yr}^{-1}$ (Morganti et al. 2005), and comparable to the starburst-driven outflow rates in massive ultraluminous infrared galaxies (e.g. Heckman 2002; Rupke et al. 2002).

3.4 Dependence on redshift and AGN luminosity

There are more than 50 detections of associated H I absorption reported in the literature, with the vast majority of the absorbers detected at low redshifts, $z < 1$ (e.g. Vermeulen et al. 2003; Gupta et al. 2006; Curran & Whiting 2010; Geréb et al. 2015). Most searches for associated H I absorption at $z > 1$ have been unsuccessful, with only five detections present in the literature. Indeed, we have earlier found evidence that the strength of H I 21 cm absorption in a uniformly-selected sample of compact flat-spectrum sources depends on both redshift and AGN luminosity, with weaker H I 21 cm absorption seen in both the high-redshift and high-luminosity sub-samples (Aditya et al. 2016). The weaker strength of H I 21 cm absorption at high redshifts might arise due to redshift evolution of the AGN environment. However, it is also possible that the observed redshift dependence of the strength of H I 21 cm absorption arises due to an underlying luminosity bias in AGN samples, as a high AGN luminosity in the ultraviolet (UV) or the radio wavebands can lead to a low H I 21 cm optical depth (e.g. Curran et al. 2008), due to either ionization of the neutral hydrogen (i.e. a lower H I column density) or changes in the hyperfine level populations (i.e. a higher spin temperature). Such a luminosity bias was indeed present in our sample of flat-spectrum sources, with the high- z AGNs having higher UV and radio luminosities (Aditya et al. 2016). It is hence not clear whether AGN luminosity or redshift evolution is the primary cause of the low observed H I 21 cm optical depths in high-redshift, high-luminosity active galactic nuclei.

There are 23 GPS sources with searches for associated H I absorption in the literature. We combined our seven targets with usable H I 21 cm absorption spectra with these systems to construct a sample of 30 GPS sources, and examined the sample for trends with redshift, rest-frame 1216 Å UV and rest-frame 1.4 GHz radio luminosities. Ta-

ble 2 summarizes the details of the sample. The luminosity at a rest-frame wavelength of 1216 Å for each AGN was estimated following the prescription of Curran et al. (2008). We first determined the flux density F_{UV} at the wavelength $1216 \times (1+z)$ Å for each AGN, by using a power-law spectrum to interpolate between its measured flux densities at two optical and/or UV wavebands in the literature. The luminosity at the rest-frame wavelength of 1216 Å was then inferred from the expression $L_{UV} = 4\pi D_{AGN}^2 F_{UV} / (1+z)$, where D_{AGN} is the luminosity distance of the AGN.

We note, in passing, that the sample of GPS sources is now formally sufficiently large (30 systems, with 10 detections of H I 21 cm absorption) to examine the dependence of the detection rate of H I 21 cm absorption on the above quantities, especially if all H I 21 cm detections are obtained at high or low values of the quantity under study. The three panels of Figure 3 plot the integrated H I 21 cm optical depth of the 30 GPS sources of the sample against redshift, rest-frame 1216 Å UV luminosity, and rest-frame 1.4 GHz radio luminosity. It is clear that the bulk of the sample is at very low redshifts and low luminosities. Indeed, the median redshift of the GPS sample is $z_{med} = 0.23$, while the median UV and radio luminosities are about an order of magnitude lower than the corresponding median values for the compact flat spectrum sample of Aditya et al. (2016). Using a Peto-Prentice two sample test, and dividing the sample at the median value of each quantity, we find no statistically-significant evidence for a dependence of the H I 21 cm absorption strength on redshift, rest-frame 1216 Å UV luminosity or rest-frame 1.4 GHz radio luminosity. However, we emphasize that our present sample of GPS sources is still relatively small, and, more important, is dominated by low-redshift, low-luminosity active galactic nuclei. Studies of the redshift evolution and luminosity dependence of the strength of H I 21 cm absorption will require significantly larger samples of GPS sources at high redshifts, $z > 1$.

3.5 Conclusions

We have used the GMRT 610 MHz receivers to detect redshifted H I 21 cm absorption from neutral gas associated with two high- z GPS sources, TXS 1200+045 at $z = 1.226$, and TXS 1245–197 at $z = 1.275$; we also report 5 new non-detections of H I 21 cm absorption at $z \approx 0.12 - 1.2$. The two new H I 21 cm absorbers have line profiles consisting of two components, narrow, deep absorption, and a wide, weak wing, with a significant part of the detected absorption blueshifted from the AGN systemic velocity, by $\approx 2300 \text{ km s}^{-1}$ for TXS 1200+045 and by $\approx 1000 \text{ km s}^{-1}$ for TXS 1245–197. In both cases, the blueshifted absorption is likely to arise from outflowing neutral gas, perhaps being driven out from the AGN environment by a galactic wind or by the radio jets. Assuming a simple wind-driven model for the outflows, we obtain relatively high mass outflow rates for the two systems, $\dot{M} \approx 18 - 32 \text{ M}_\odot \text{ yr}^{-1}$, assuming a gas spin temperature of 1000 K.

Including 23 GPS sources that have earlier searches for associated H I 21 cm absorption available in the literature, we have constructed a sample of 30 GPS sources, and examined the trends of H I 21 cm absorption strength with redshift, rest-frame 1216 Å UV and rest-frame 1.4 GHz radio luminosity. Unlike in the case of earlier H I 21 cm absorption studies

of samples of compact flat-spectrum sources, we do not find statistically-significant evidence for the hypothesis that the strength of H I 21 cm absorption in our sample depends on redshift or rest-frame AGN 1216 Å UV or 1.4 GHz radio luminosity. This is likely to be because our GPS sample is both relatively small and dominated by low-redshift, low-luminosity active galactic nuclei.

ACKNOWLEDGEMENTS

We thank the staff of the GMRT who have made these observations possible. The GMRT is run by the National Centre for Radio Astrophysics of the Tata Institute of Fundamental Research. NK acknowledges support from the Department of Science and Technology via a Swarnajayanti Fellowship (DST/SJF/PSA-01/2012-13). We thank an anonymous referee for a very helpful report on an earlier draft that significantly improved the quality of this paper.

REFERENCES

- Abazajian K., et al., 2005, *AJ*, 129, 1755
Abazajian K. N., et al., 2009, *ApJS*, 182, 543
Adelman-McCarthy J. K., et al., 2008, *ApJS*, 175, 297
Aditya J. N. H. S., Kanekar N., Kurapati S., 2016, *MNRAS*, 455, 4000
Aditya J. N. H. S., Kanekar N., Prochaska J. X., Day B., Lynam P., Cruz J., 2017, *MNRAS*, 465, 5011
Alatalo K., et al. 2011, *ApJ*, 735, 88
Becker R. H., White R. L., Helfand D. J., 1995, *ApJ*, 450, 559
Bianchi L., Conti A., Shiao B., 2014, *Advances in Space Research*, 53, 900
Carilli C. L., Menten K. M., Reid M. J., Rupen M. P., Yun M. S., 1998, *ApJ*, 494, 175
Chandola Y., Sirothia S. K., Saikia D. J., 2011, *MNRAS*, 418, 1787
Combes F., et al., 2013, *A&A*, 558, A124
Condon J. J., Cotton W. D., Greisen E. W., Yin Q. F., Perley R. A., Taylor G. B., Broderick J. J., 1998, *AJ*, 115, 1693
Croton D. J., et al., 2006, *MNRAS*, 365, 11
Curran S. J., Whiting M. T., 2010, *ApJ*, 712, 303
Curran S. J., Whiting M. T., Wiklind T., Webb J. K., Murphy M. T., Purcell C. R., 2008, *MNRAS*, 391, 765
Curran S. J., Whiting M. T., Sadler E. M., Bignell C., 2013, *MNRAS*, 428, 2053
Dasra K. M., Combes F., Oosterloo T., Oonk J. B. R., Morganti R., Salomé P., Vlahakis N., 2016, *A&A*, 595, L7
Douglas J. N., Bash F. N., Bozayan F. A., Torrence G. W., Wolfe C., 1996, *AJ*, 111, 1945
Fabian A. C., 2012, *ARA&A*, 50, 455
Fanti C., Fanti R., Dallacasa D., Schilizzi R. T., Spencer R. E., Stanghellini C., 1995, *A&A*, 302, 317
Fiore F., et al., 2017, *A&A*, 601, A143
Geréb K., Maccagni F. M., Morganti R., Oosterloo T. A., 2015, *A&A*, 575, A44
Gupta N., Salter C. J., Saikia D. J., Ghosh T., Jeyakumar S., 2006, *MNRAS*, 373, 972
Gupta N., Srianand R., Petitjean P., Bergeron J., Noterdaeme P., Muzahid S., 2012, *A&A*, 544, 21
Heckman T. M., 2002, in Mulchaey J. S., Stocke J. T., eds, *Astronomical Society of the Pacific Conference Series Vol. 254, Extragalactic Gas at Low Redshift*. p. 292
Hewett P. C., Wild V., 2010, *MNRAS*, 405, 2302
Hopkins P. F., Hernquist L., Cox T. J., Di Matteo T., Martini P., Robertson B., Springel V., 2005, *ApJ*, 630, 705
Ishwara-Chandra C. H., Dwarakanath K. S., Anantharamaiah K. R., 2003, *Journal of Astrophysics and Astronomy*, 24, 37
Kanekar N., 2014, *ApJL*, 797, L20
Kanekar N., Subrahmanyan R., Ellison S. L., Lane W. M., Chengalur J. N., 2006, *MNRAS*, 370, L46
Kanekar N., Chengalur J. N., Lane W. M., 2007, *MNRAS*, 375, 1528
Kanekar N., Prochaska J. X., Ellison S. L., Chengalur J. N., 2009, *MNRAS*, 396, 385
Labiano A., Barthel P. D., O’Dea C. P., de Vries W. H., Pérez I., Baum S. A., 2007, *A&A*, 463, 97
Liu X., Cui L., Luo W.-F., Shi W.-Z., Song H.-G., 2007, *A&A*, 470, 97
Maloney P. R., Hollenbach D. J., Tielens A. G. G. M., 1996, *ApJ*, 466, 561
Monet D. G., et al., 2003, *AJ*, 125, 984
Moore C. B., Carilli C. L., Menten K. M., 1999, *ApJ*, 510, L87
Morganti R., 2012, *Astrophysics and Space Science Proceedings*, 25, 31
Morganti R., Oosterloo T., Tsvetanov Z., 1998, *AJ*, 115, 915
Morganti R., Oosterloo T. A., Emonts B. H. C., van der Hulst J. M., Tadhunter C. N., 2003, *ApJL*, 593, L69
Morganti R., Tadhunter C. N., Oosterloo T. A., 2005, *A&A*, 444, L9
Morganti R., Veilleux S., Oosterloo T., Teng S. H., Rupke D., 2016, *A&A*, 593, A30
O’Dea C. P., 1998, *PASP*, 110, 493
Oosterloo T. A., Morganti R., Tzioumis A., Reynolds J., King E., McCulloch P., Tsvetanov Z., 2000, *AJ*, 119, 2085
Peck A. B., Taylor G. B., Conway J. E., 1999, *ApJ*, 521, 103
Pihlström Y. M., Conway J. E., Vermeulen R. C., 2003, *A&A*, 404, 871
Randall K. E., Hopkins A. M., Norris R. P., Edwards P. G., 2011, *MNRAS*, 416, 1135
Readhead A. C. S., Taylor G. B., Pearson T. J., Wilkinson P. N., 1996, *ApJ*, 460, 634
Rengelink R. B., Tang Y., de Bruyn A. G., Miley G. K., Bremer M. N., Roettgering H. J. A., Bremer M. A. R., 1997, *A&AS*, 124
Rupke D. S., Veilleux S., Sanders D. B., 2002, *ApJ*, 570, 588
Saikia D. J., Gupta N., Konar C., 2007, *MNRAS*, 375, L31
Snellen I. A. G., Schilizzi R. T., Miley G. K., de Bruyn A. G., Bremer M. N., Röttgering H. J. A., 2000, *MNRAS*, 319, 445
Sokolovsky K. V., Kovalev Y. Y., Pushkarev A. B., Mimica P., Perucho M., 2011, *A&A*, 535, A24
Springel V., Di Matteo T., Hernquist L., 2005, *MNRAS*, 361, 776
Stanghellini C., O’Dea C. P., Dallacasa D., Baum S. A., Fanti R., Fanti C., 1998, *A&AS*, 131, 303
Surace J. A., Sanders D. B., 2000, *AJ*, 120, 604
Usun J. M., Bagri D. S., Cornwell T. J., 1991, *Physical Review Letters*, 67, 3328
Veilleux S., Cecil G., Bland-Hawthorn J., 2005, *ARA&A*, 43, 769
Vermeulen R. C., et al., 2003, *A&A*, 404, 861
Véron-Cetty M.-P., Woltjer L., Staveley-Smith L., Ekers R. D., 2000, *A&A*, 362, 426
Wagner A. Y., Bicknell G. V., 2011, *ApJ*, 728, 29
Wagner A. Y., Bicknell G. V., Umemura M., 2012, *ApJ*, 757, 136
Wilkinson P. N., Polatidis A. G., Readhead A. C. S., Xu W., Pearson T. J., 1994, *ApJ*, 432, L87
Wolfe A. M., Briggs F. H., Davis M. M., 1982, *ApJ*, 259, 495
Wolfe A. M., Briggs F. H., Turnshek D. A., Davis M. M., Smith H. E., Cohen R. D., 1985, *ApJ*, 294, L67
Zacharias N., Monet D. G., Levine S. E., Urban S. E., Gaume R., Wycoff G. L., 2004, in *American Astronomical Society Meeting Abstracts*. p. 1418

- de Vries N., Snellen I. A. G., Schilizzi R. T., Lehnert M. D.,
Bremer M. N., 2007a, [A&A](#), 464, 879
- de Vries N., Snellen I. A. G., Schilizzi R. T., Lehnert M. D.,
Bremer M. N., 2007b, [A&A](#), 464, 879
- van Gorkom J. H., Knapp G. R., Ekers R. D., Ekers D. D., Laing
R. A., Polk K. S., 1989, *AJ*, 97, 708

This paper has been typeset from a $\text{\TeX}/\text{\LaTeX}$ file prepared by
the author.